

WRF-GS: Wireless Radiation Field Reconstruction with 3D Gaussian Splatting

Chaozheng Wen, Jingwen Tong, Yingdong Hu, Zehong Lin, and Jun Zhang, *Fellow, IEEE*

Abstract—Wireless channel modeling plays a pivotal role in designing, analyzing, and optimizing wireless communication systems. Nevertheless, developing an effective channel modeling approach has been a longstanding challenge. This issue has been escalated due to the denser network deployment, larger antenna arrays, and wider bandwidth in 5G and beyond networks. To address this challenge, we put forth WRF-GS, a novel framework for channel modeling based on wireless radiation field (WRF) reconstruction using 3D Gaussian splatting. WRF-GS employs 3D Gaussian primitives and neural networks to capture the interactions between the environment and radio signals, enabling efficient WRF reconstruction and visualization of the propagation characteristics. The reconstructed WRF can then be used to synthesize the spatial spectrum for comprehensive wireless channel characterization. Notably, with a small number of measurements, WRF-GS can synthesize new spatial spectra within milliseconds for a given scene, thereby enabling latency-sensitive applications. Experimental results demonstrate that WRF-GS outperforms existing methods for spatial spectrum synthesis, such as ray tracing and other deep-learning approaches. Moreover, WRF-GS achieves superior performance in the channel state information prediction task, surpassing existing methods by a significant margin of more than 2.43 dB.

Index Terms—Wireless channel modeling, wireless radiation field reconstruction, 3D Gaussian splatting, channel prediction.

I. INTRODUCTION

Modern communications increasingly depend on wireless technologies that use electromagnetic (EM) waves for information exchange, driving advancements in mobile phones, automotive systems, and Internet-of-Thing devices [1]. At the core of these innovations lies *wireless channel modeling*, a long-standing problem in wireless communications. While the physics of EM wave propagation is described by Maxwell’s equations [2], solving these equations in reality is intricate due to the need for comprehensive knowledge of boundary conditions. This complexity has led to the development of various wireless channel modeling approaches, as shown in Fig. 1, which can be categorized into probabilistic modeling, deterministic modeling, and neural modeling.

The probabilistic models rely on statistical methods to predict channel characteristics, primarily estimating the received signal strength based on the distance between the transmitter (TX) and receiver (RX). These models are based on empirical

This work was supported by the Hong Kong Research Grants Council under the Areas of Excellence scheme grant AoE/E-601/22-R and NSFC/RGC Collaborative Research Scheme grant CRS_HKUST603/22.

The authors are with the Department of Electronic and Computer Engineering, Hong Kong University of Science and Technology, Hong Kong (E-mails: cwena@connect.ust.hk, eejwentong@ust.hk, yhudj@connect.ust.hk, eezhlin@ust.hk, eejzhang@ust.hk). (Corresponding authors: Jingwen Tong; Zehong Lin.)

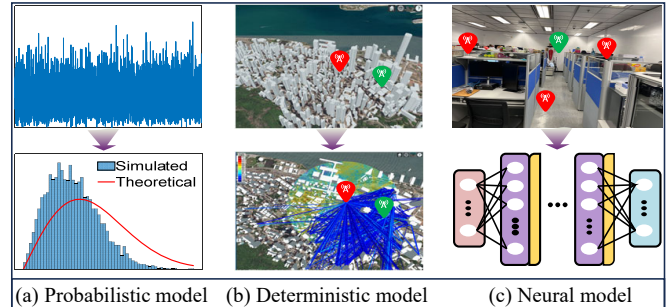


Fig. 1: Different types of wireless channel modeling.

formulas and use measurements to calibrate parameters for typical scenarios [3]. However, they often lack accuracy and struggle to provide detailed channel characteristics. For example, in multi-antenna systems, the probabilistic models fail to characterize the energy distribution of the received signal from all directions, i.e., to reconstruct the *spatial spectrum* of the received signal by estimating its angle of arrival (AoA). To overcome these drawbacks, the deterministic models use physical principles to predict channel characteristics under an approximate environmental model. For example, the ray tracing method generates propagation characteristics based on computer-aided design representations of the environment, including object boundaries and material reflection coefficients [4]. Therefore, these models can provide more comprehensive channel information than probabilistic models. However, their accuracy may be compromised, as they cannot capture the detailed physical characteristics of the environment.

In contrast, the neural models, adopting the data-driven principle, learn the complex interactions between the environment and radio signals directly from location-based data, rather than relying on predefined statistical or physical models. One of the promising advancements in neural models is the recent adoption of the neural radiance field (NeRF), a breakthrough in computer vision for view synthesis [5]. Motivated by the fact that light is a kind of EM wave, Refs. [6] and [7] proposed two NeRF-based frameworks, named NeRF² and NeWRF, respectively, for wireless channel modeling based on implicit *wireless radiation field* (WRF) reconstruction. The reconstructed WRF can provide detailed and accurate channel characteristics and significantly enhance communication performance. However, these methods suffer from high computational complexity and slow synthesis (a.k.a. rendering) speeds. In practice, the synthesis operation corresponds to the channel characteristic prediction process and will significantly affect the round-trip time in communication systems, which is

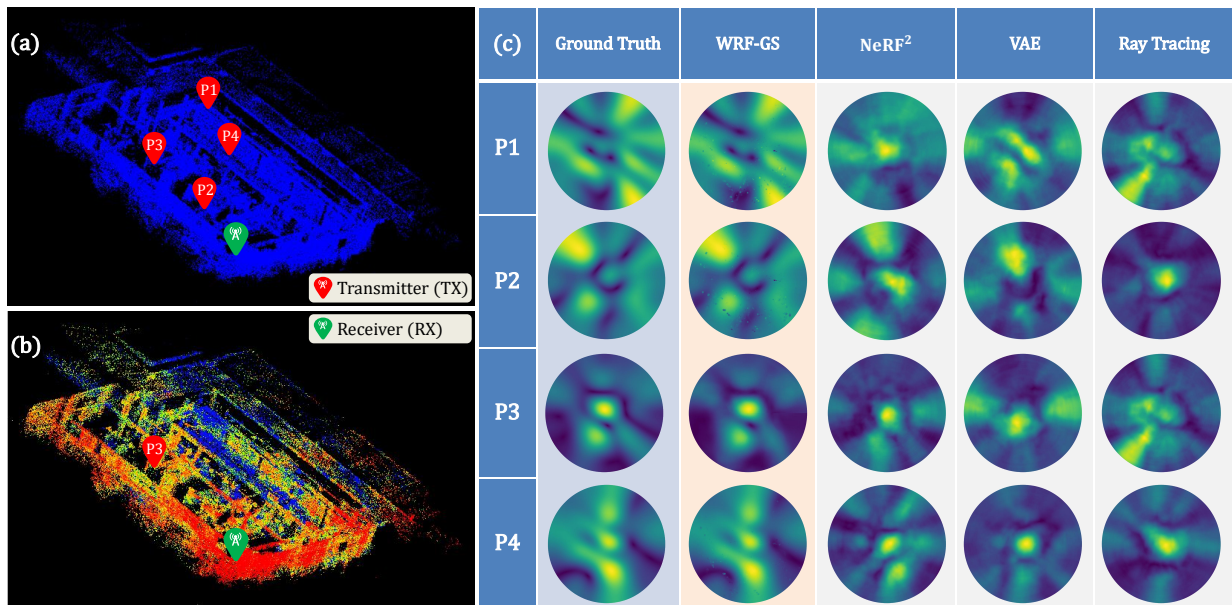


Fig. 2: The synthesized spatial spectrum of different algorithms in a laboratory environment. The spatial spectrum represents the signal strength received from different directions composed of the azimuthal and elevation angles. (a) shows the 3D point clouds of the laboratory created by LiDAR, which are used for the ray-tracing algorithm. In addition, the TX can be located at any position, and the RX is equipped with a 4×4 antenna array and fixed at a corner; (b) is a reconstructed WRF when the TX is located at P3 by running the WRF-GS framework using the 3D point clouds in (a) as initialization. The spatial spectrum is obtained by a series of nonlinear transformations, such as projecting the WRF onto the hemispherical plane, where the colors of the points represent different degrees of contribution to the spatial spectrum. (c) compares the synthesized spatial spectra of four algorithms when the TX is located at four different positions, i.e., P1-P4, as shown in (a). The ground truth is obtained using the antenna array.

critical for latency-sensitive applications. For instance, cloud gaming and digital twins typically demand low latency, i.e., under 20 milliseconds for cloud gaming [8] and often within a few milliseconds for digital twins [9]. This renders the NeRF-based methods impractical.

To conquer this challenge, we propose WRF-GS, a hybrid framework for fast and accurate channel modeling based on explicit WRF reconstruction using neural networks and 3D Gaussian splatting (3D-GS). 3D-GS utilizes an analytical architecture to represent and render 3D scenes, enabling high-quality and real-time view synthesis [10]. Compared with NeRF, 3D-GS offers faster rendering speeds and lower computational complexity. By adapting 3D-GS from the optical domain to the radio-frequency (RF) domain, WRF-GS can predict the received signal at any location within milliseconds for a give scene after training with a small number of signal measurements. Fig. 2 illustrates the synthesized spatial spectra of four algorithms based on the reconstructed WRF in a laboratory environment when the RX is fixed at one position and the TX is located at four different positions (i.e., P1-P4). Evidently, WRF-GS has the best prediction accuracy compared with the baselines, closely matching the ground truth.

Nevertheless, directly applying the optical 3D-GS technique to the RF domain poses several challenges. First, the optical 3D-GS only considers the amplitude (i.e., light strength) of the optical signal, while the received RF signal consists of both amplitude and phase components, as EM waves are more prone to reflection, diffraction, and scattering than lights. Second, the measurement of visible light is via a million-pixel camera, but an RX typically utilizes either a single antenna or an antenna array. Third, the rendering function

in the RF domain differs from the optical 3D-GS due to the unique physics of EM wave propagation. To address these challenges, we propose WRF-GS, a novel framework that refines the optical 3D-GS technique [10] from three key aspects. **Scenario Representation Network:** We introduce two multi-layer perceptions (MLPs) to effectively capture the complex interactions between the environment and radio signals. The learned features are then embedded into 3D Gaussian points, which serve as virtual TXs in wireless propagation. **Projection Model:** We devise a projection model to transform the optical camera model into an RF antenna model using spherical and Mercator projections. This model projects the virtual TXs onto the RX perception plane. **Electromagnetic Splatting:** Based on the projected 3D Gaussian points, we employ a differentiable tile rasterizer to synthesize wireless channel characteristics. This operation enables rapid synthesis of new channel characteristics within milliseconds.

We conduct extensive experiments to evaluate the performance of the proposed WRF-GS. Unlike NeRF-based approaches that adopt an implicit representation, our WRF-GS explicitly represents the propagation characteristics, as shown in Fig. 2 (b). In addition, WRF-GS achieves higher reconstruction accuracy, higher sample efficiency, and faster rendering speed. Furthermore, we consider a downlink channel state information (CSI) prediction task in a multiple-input-multiple-output (MIMO) system as a case study to further demonstrate the effectiveness of WRF-GS in practical systems. Our results show that WRF-GS achieves better prediction performance of the downlink CSI than the baselines, outperforming NeRF² by a significant margin of 2.43 dB.

In summary, this paper makes the following contributions:

i) We propose WRF-GS, a hybrid framework tailored for wireless channel modeling based on WRF reconstruction using neural networks and 3D-GS; ii) We adapt the optical 3D-GS to the RF domain by designing the modules of scenario representation network, projection model, and electromagnetic splatting. The integration of the EM wave physics and 3D-GS enables a visible, low-cost, and accurate channel modeling approach; iii) We conduct extensive experiments and a case study to demonstrate the effectiveness of WRF-GS. Numerical results show that WRF-GS outperforms existing methods.

II. RELATED WORKS

Wireless channel modeling involves measuring and characterizing the propagation of EM waves between TXs and RXs, taking into account various phenomena such as reflection, diffraction, scattering, and path loss [11], [12]. Sarkar *et al.* [3] surveyed various propagation models for mobile communications using statistical methods to describe the random nature of EM wave propagation. To provide more detailed channel characteristics, Oestges *et al.* [11] applied the ray tracing technique to simulate the paths of EM waves, which allows for precise predictions and accounts for large-scale features of the environment. These methods, however, fail to capture the materials and physical characteristics of the environment.

Environment-aware channel modeling has attracted much attention since future wireless networks will generate abundant location-specific channel data and are expected to possess more powerful data mining and AI capabilities [13], [14]. This motivated the adaptation of neural networks for more accurate channel modeling, i.e., learning the complex interactions between the environment and radio signals directly from location-based data [15]. To achieve this goal, a few recent works have been devoted to NeRF-based wireless channel modeling [6], [7], [16]. Orekondy *et al.* [16] proposed a neural surrogate to model wireless EM propagation effects in indoor environments based on NeRF using two synthetic datasets. Meanwhile, Zhao *et al.* [6] presented NeRF² for spatial spectrum reconstruction in a real-world environment. By fixing a TX at an indoor location, Lu *et al.* [7] presented NeWRF, a NeRF-based wireless channel prediction framework with a sparse set of channel measurements. However, NeRF-based methods often suffer from high computational complexity and slower synthesis speed. In this paper, we present WRF-GS for environment-aware channel modeling with 3D-GS, reconciling the accuracy and computational complexity.

CSI prediction involves estimating future channel conditions based on current and historical data. Existing studies have been dedicated to predicting downlink channel states by observing uplink channels, as both are influenced by the same underlying physical environment and traverse identical paths [17]–[19]. Liu *et al.* [17] introduced FIRE, a variational auto-encoder (VAE) method, to transfer estimated CSI from the uplink to the downlink. In addition, Vasishth *et al.* [18] and Bakshi *et al.* [19] proposed R2F2 and OptML to predict the CSI using machine learning-based methods. In this paper, we

apply WRF-GS to the CSI prediction task by transferring the estimated CSI from uplink to downlink.

III. PRELIMINARIES

In this section, we present preliminaries on wireless channel modeling and 3D Gaussian Splatting.

A. Wireless Channel Modeling

A generic wireless communication system typically consists of a TX that generates and modulates an information signal, which is then transmitted through the wireless channel to an RX. The transmitted signal can be represented as a complex number $s = Ae^{j\varphi}$, where A and φ denote the amplitude and phase of the transmitted signal, respectively. In the wireless medium, the propagation of EM signals is characterized by key phenomena such as path loss and multipath propagation. For the basic free space path loss model, the received signal y at the RX is given by

$$y = Ae^{j\varphi} \cdot \Delta A e^{j\Delta\varphi}, \quad (1)$$

where ΔA and $\Delta\varphi$ are the amplitude attenuation factor and phase rotation experienced by the signal, respectively. Due to various propagation effects, including reflection, scattering, refraction, and diffraction, the received signal is the sum of multiple copies of the transmitted signal. Consequently, it is more generally expressed as

$$y = Ae^{j\varphi} \sum_{l=0}^{L-1} \Delta A_l e^{j\Delta\varphi_l}, \quad (2)$$

where L is the total number of propagation paths, and ΔA_l and $\Delta\varphi_l$ represent the amplitude attenuation factor and phase rotation associated with the l -th path, respectively.

In multi-antenna systems, an antenna array is employed to characterize the energy distribution of the received signal y from all directions, i.e., to estimate the AoA of the received signal. To illustrate this concept, we consider an antenna array equipped with $\sqrt{K} \times \sqrt{K}$ antennas, as depicted in Fig. 3. The spacing of two adjacent antennas is D , which is less than the wavelength λ . As shown in Fig. 3(b), the antenna array receives signals in a hemispherical plane to provide omnidirectional coverage and to efficiently capture signals from various directions. The direction of an RF source is characterized by the azimuthal angle α and elevation angle β , where $0^\circ \leq \alpha < 360^\circ$ and $0^\circ \leq \beta < 90^\circ$. The phase difference between the signals received by the (m, n) -th antenna pair is related to the distance of the two antennas from the source [20], i.e.,

$$\begin{aligned} \Delta\theta_{m,n} &= \text{mod} \left(\frac{2\pi\Delta d_{m,n}}{\lambda}, 2\pi \right) \\ &= \text{mod} \left(\frac{-2\pi r_{m,n} \cos(\alpha - \phi_{m,n}) \cos(\beta)}{\lambda}, 2\pi \right), \end{aligned}$$

where $\Delta d_{m,n}$ is shown in Fig. 3(a) and can be computed by $\Delta d_{m,n} = |BA_{m,n}| - |BA_{0,0}| = -r_{m,n} \cos(\alpha - \phi_{m,n}) \cos\beta$,

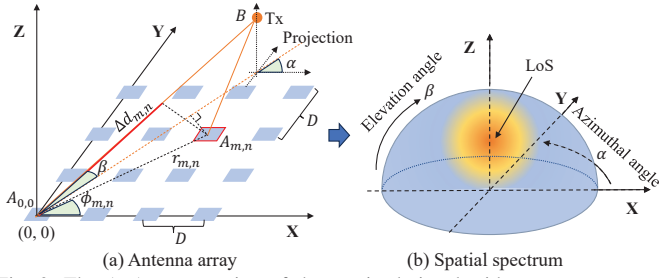


Fig. 3: The AoA computation of the received signal with an antenna array. (a) There are K antennas deployed in a grid, and the signal source is located at point B. (b) The spatial spectrum is generated from the antenna array. The illustration of spatial spectrum in Fig. 2(c) is obtained by projecting the spatial spectrum to the X-Y plane.

and $m, n = 0, \dots, \sqrt{K} - 1$. In addition, $r_{m,n} = D\sqrt{m^2 + n^2}$ and $\phi_{m,n} = \arctan 2(n, m)$ are the radius and angle of antenna $A_{m,n}$ at the polar coordinate system, respectively.

The AoA of the received signal is calculated by comparing the phases of signals received from multiple antennas. For AoA estimation, we use the antenna array to form a very narrow beam and steer it. When the beam is steered in the line-of-sight (LoS) direction, the array effectively blocks power from all other directions. This allows to reconstruct the spatial spectrum by steering the beam across a grid of azimuth and elevation angles and measuring the received signal power at each pointing direction. Specifically, we can form a matrix \mathbf{P} , where each element $P(\alpha, \beta)$ represents the power of the received signal from the azimuthal angle α and elevation angle β , i.e.,

$$P(\alpha, \beta) = \left| \frac{1}{K} \sum_{m,n=0}^{\sqrt{K}-1, \sqrt{K}-1} e^{j(\Delta\hat{\theta}_{m,n} - \Delta\theta_{m,n})} \right|^2, \quad (3)$$

and

$$\Delta\hat{\theta}_{m,n} = \hat{\theta}_{m,n} - \hat{\theta}_{0,0},$$

where $\hat{\theta}_{m,n}$ denotes the measured phase of the RF signal received at the antenna $A_{m,n}$, and $\hat{\theta}_{0,0}$ is a constant term. Considering a one-degree angular resolution, the spatial spectrum can be reconstructed as a 360×90 matrix:

$$\mathbf{P} = \begin{bmatrix} P(0^\circ, 0^\circ) & P(1^\circ, 0^\circ) & \dots & P(359^\circ, 0^\circ) \\ P(0^\circ, 1^\circ) & P(1^\circ, 1^\circ) & \dots & P(359^\circ, 1^\circ) \\ \vdots & \vdots & \ddots & \vdots \\ P(0^\circ, 89^\circ) & P(1^\circ, 89^\circ) & \dots & P(359^\circ, 89^\circ) \end{bmatrix}. \quad (4)$$

In summary, the reconstructed spatial spectrum can be interpreted as a spatial power distribution function, which directly corresponds to the WRF emitting from the transmitting source and propagating through the environment. In other words, the spatial spectrum serves as a representation of the underlying WRF, providing valuable insights into wireless channel modeling. Therefore, this paper aims to reconstruct the WRF and synthesize the spatial spectrum using the 3D-GS technique, which is introduced in the next subsection.

B. 3D Gaussian Slapping

3D-GS is a technique that utilizes a set of 3D Gaussian functions to model the geometry and appearance of a scene,

offering a compact and efficient representation [10]. Unlike the computationally intensive and memory-heavy NeRF approach [5], 3D-GS provides a more lightweight and scalable solution for scene representation. Mathematically, 3D-GS provides a novel way to represent space using anisotropic Gaussian primitives, where each Gaussian is characterized by its own covariance matrix $\Sigma \in \mathbb{R}^{3 \times 3}$ and center position vector $\mu \in \mathbb{R}^3$. The 3D Gaussian distribution can be expressed as

$$G(\mathbf{x}) = e^{-\frac{1}{2}(\mathbf{x}-\mu)^T \Sigma^{-1}(\mathbf{x}-\mu)}, \quad (5)$$

where $\mathbf{x} = (x_0, x_1, x_2)$ represents the three-dimensional spatial position of the Gaussian point, and Σ can be expressed in terms of a scaling matrix \mathbf{S} and a rotation matrix \mathbf{R} as

$$\Sigma = \mathbf{R}\mathbf{S}\mathbf{S}^T\mathbf{R}^T. \quad (6)$$

The rendering process begins by transforming the 3D Gaussians $G(\mathbf{x})$ in space into 2D Gaussians $G'(\mathbf{x}')$ on the image plane [21]. These 2D Gaussians are then sorted based on their depth information. Each tile is processed independently and in parallel for the 2D Gaussians in its coverage. Utilizing the opacity o_i and color attribute c_i of each Gaussian, alpha blending is applied to the color values on each pixel:

$$C = \sum_{i=1}^N c_i \alpha_i \prod_{j=1}^{i-1} (1 - \alpha_j) \text{ and } \alpha_i = o_i G'_i(\Delta \mathbf{p}_i), \quad (7)$$

where N is the number of 3D Gaussians near a given pixel, and $\Delta \mathbf{p}_i = \mathbf{p}_i - \mathbf{p}_s$ is the difference vector between the projected center \mathbf{p}_i of a Gaussian and the sampling pixel position \mathbf{p}_s . Once the color of each pixel is computed, the entire image is rendered. Subsequently, a comparison is made with the ground truth image to calculate the pixel-wise loss, which is then used to optimize the parameters of the model.

IV. THE WRF-GS FRAMEWORK

In this section, we present the WRF-GS framework for wireless channel modeling based on WRF reconstruction using 3D-GS. This novel framework harnesses the power of 3D-GS and adapts it from the optical domain to the RF domain. The key insight is to convert the space particles into virtual TXs using a continuous volumetric scene function in 3D-GS.

A. Problem Description and Framework Overview

We consider a scenario comprising a TX, an RX equipped with an antenna array, and various obstacles such as floors, walls, and furniture. The RX is placed at a fixed position, while the TX is randomly positioned in the space. Following [6], we assume that the distribution of main obstacles in the space is fixed, and any temporary perturbations caused by moving small obstacles are mitigated through techniques like Kalman filtering to minimize their impact. As described in Section III-A, the received signal is the superposition of sub-signals from multiple propagation paths. Each sub-signal can be represented as an LoS signal from a virtual TX. Our objective is to reconstruct the spatial power spectrum received at the RX antenna array by synthesizing the distribution of these virtual TXs within the scenario.

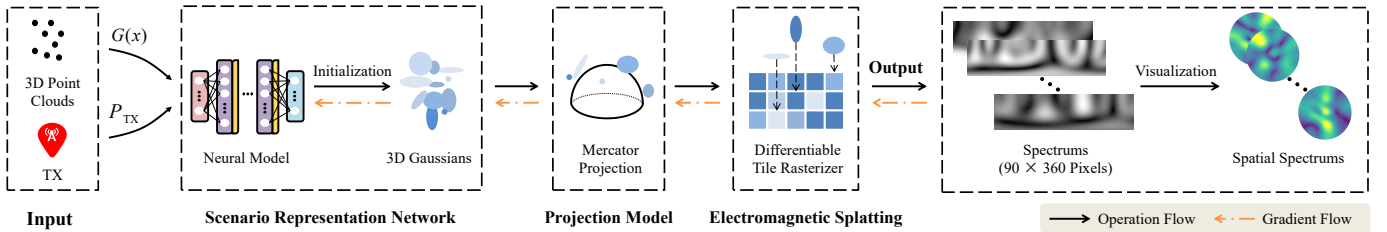


Fig. 4: An overview of the WRF-GS framework. The 3D point clouds, which can be randomly distributed or captured via LiDAR sensors, and the position of the TX are first passed into a scenario representation network. This network represents the virtual TXs in the scene using a set of 3D Gaussians, each of which carries environmental attenuation information and signal characteristics. To project these 3D Gaussian representations onto the perception plane of the RX antenna array, the Mercator projection is employed. Finally, the resulting spatial spectra are rendered using the electromagnetic splatting method.

This task is analogous to the optical 3D-GS technique that explicitly models the distribution of particles in a scene to enable arbitrary view synthesis [10]. This motivates us to employ 3D-GS to reconstruct the WRF and propose a novel framework named WRF-GS. Specifically, WRF-GS aims to model the virtual TX distribution to synthesize the received spatial spectrum by combining the EM wave physics and 3D-GS. Since 3D Gaussians possess attributes such as volume, color, and opacity, and serve as the fundamental building blocks in the representation space, they can be naturally translated into virtual TXs in the RF domain. During EM propagation, the overall outcome is perceived as the combined effect of the signal and attenuation, as described in Eqn. (2). In this context, the color attribute is replaced by the signal strength, while the opacity corresponds to the attenuation.

Nevertheless, the projection and splatting of WRF reconstruction in 3D-GS are distinct from the optical domain described in Section III-B. In optical 3D-GS, the goal is to project 3D Gaussian particles representing objects onto the camera’s 2D image plane. This involves applying a coordinate projection transformation that accounts for the camera’s position, orientation, and intrinsic parameters. In contrast, the RF domain requires mapping the virtual TXs represented by 3D Gaussians onto a perception plane of the RX antenna array. Since the RX antenna array receives signals in a hemispherical plane, as discussed in Section III-A, a new projection approach is required to map the 3D Gaussians onto a hemispherical plane, rather than a flat 2D plane. This operation is crucial for aligning the virtual TXs with the specific direction of the RX antenna array. Furthermore, in optical 3D-GS, the rendered image is generated by the splatted Gaussians, including volume, color, and opacity. While the 3D Gaussian attributes in the RF domain represent the signal strength and attenuation. This necessitates a new splatting process to blend the contributions of all the virtual TXs, accounting for their signal strengths and attenuation, to synthesize the received spatial power spectrum.

Our proposed WRF-GS effectively addresses the above challenges and enables the reconstruction of the spatial spectrum. The overall structure of WRF-GS is illustrated in Fig. 4. It takes the positions of physical TXs and 3D point clouds as input and outputs the spatial spectrum at the RX antenna array. WRF-GS consists of the following three core modules:

- **Scenario Representation Network:** This module is responsible for representing the virtual TXs using 3D Gaussians.

By processing the input data, the 3D Gaussians capture the signal strength and attenuation properties, which enables the synthesis of the WRF in the environment.

- **Projection Model:** This model projects the virtual TXs represented by 3D Gaussians onto the perception plane of the RX antenna array. To account for the hemispherical nature of the antenna’s reception, we employ the Mercator projection to achieve this spatial projection.
- **Electromagnetic Splatting:** Based on the properties of 3D Gaussians and the characteristics of EM wave propagation in space, we employ a hardware acceleration algorithm to efficiently process and combine the contributions of the virtual TXs onto the RX antenna array, ultimately synthesizing the received spatial spectrum.

In the following, we elaborate on these three modules.

B. Scenario Representation Network

The scenario representation network plays a crucial role in modeling the underlying relationships between the environment and radio signals by representing the virtual TXs as 3D Gaussians using two MLPs. The network architecture, depicted in Fig. 5, follows the DeepSDF structure [22].

To capture the attenuation, which solely depends on the spatial location, we initially feed the positions of the initial point clouds (equivalent to the center coordinates of the 3D Gaussians $G(\mathbf{x})$) into a network consisting of eight fully connected layers. Each layer comprises ReLU activations and 128 channels. The output of this network provides the attenuation $\delta(\mathbf{x})$ of each input 3D Gaussian $G(\mathbf{x})$ at the corresponding position \mathbf{x} and a feature vector. Subsequently, we pass this feature vector, along with the TX position P_{TX} , through another two-layer fully connected network (with ReLU activations and 128 and 64 channels, respectively). The final output is the signal $S(\mathbf{x})$ that represents the 3D Gaussian signal associated with the virtual TX at position \mathbf{x} . Therefore, for each 3D Gaussian $G(\mathbf{x})$ representing a virtual TX, we obtain the corresponding signal $S(\mathbf{x})$ and attenuation $\delta(\mathbf{x})$ from the scenario representation network, i.e.,

$$F_{\Theta} : (G(\mathbf{x}), P_{\text{TX}}) \Rightarrow (\delta(\mathbf{x}), S(\mathbf{x})), \quad (8)$$

where Θ denotes the learnable neural network weights. Considering that signals and attenuation in space are typically expressed as complex numbers, as shown in Eqn. (1), the two outputs here are denoted by $\delta(\mathbf{x}) = \Delta A(\mathbf{x})e^{j\Delta\psi(\mathbf{x})}$ and

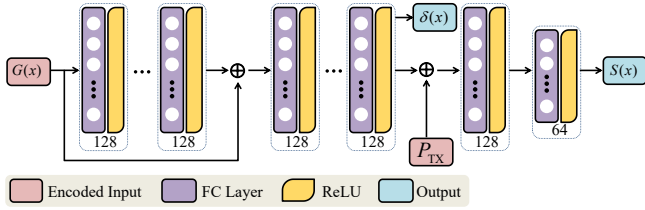


Fig. 5: Architecture of the neural model. The model comprises two MLPs. The first MLP processes the input 3D point clouds to capture the spatial attenuation information of the environment, which is independent of the specific TX position. This MLP outputs the attenuation and a feature vector for each spatial location. The second MLP then combines the spatial feature vector with the TX position to capture the signal characteristics.

$S(\mathbf{x}) = A(\mathbf{x})e^{j\psi(\mathbf{x})}$, respectively, where $A(\mathbf{x})$ represents the amplitude and $\psi(\mathbf{x})$ represents the phase.

This network is specifically designed to transform the 3D point clouds and TX position information into the signal and attenuation properties of 3D Gaussians, respectively. Unlike DeepSDF, which is typically applied to optics and assumes a fixed TX (light source) position, our network is designed to handle mobile TXs. Moreover, the outputs are all complex-valued signals that incorporate additional phase information. This unique feature enables our model to successfully represent both the signal characteristics of virtual TXs in space and the attenuation information of the surrounding environment.

C. Projection Model

The projection model maps the virtual TXs represented by 3D Gaussians onto the perception plane of the RX antenna array. There are several key differences compared with the camera model in optical 3D-GS. Unlike pinhole or fisheye cameras, the antenna in our WRF-GS receives signals from a hemispherical direction. In addition, we do not need to know the distortion caused by coordinate transformation. This is because we only care about the signal at the corresponding angular resolution and ignore the signal between angles. Moreover, as shown in Eqn. (4), the arrangement of pixels in the final spatial spectrum differs from conventional photographs that adhere to human visual perception.

To project a 3D point $\mathbf{t} = [t_x, t_y, t_z]^T$ onto the perception plane of the RX antenna array at $\mathbf{p} = [p_x, p_y]^T$, we employ the Mercator projection, a widely used orthographic cylindrical projection in cartography. This allows us to map the latitude and longitude grid of a sphere onto a cylindrical surface, which can then be unrolled onto a flat plane. We define a right-handed Cartesian coordinate at the receiving end of the antenna, with the antenna array oriented in the positive Z-direction and the signal being received in a spherical plane, as shown in Fig. 6(a). Using longitude Ω_{lon} and latitude Ω_{lat} , we can concisely and accurately represent positional relationships in space, which is expressed using inverse trigonometric functions as:

$$\begin{bmatrix} \Omega_{\text{lon}} \\ \Omega_{\text{lat}} \end{bmatrix} = \begin{bmatrix} \arctan 2(t_y/t_x) \\ \arcsin(t_z/t_r) \end{bmatrix}, \quad (9)$$

where $t_r = \sqrt{t_x^2 + t_y^2 + t_z^2}$ denotes the distance from the center coordinate of the 3D Gaussian in space to the center

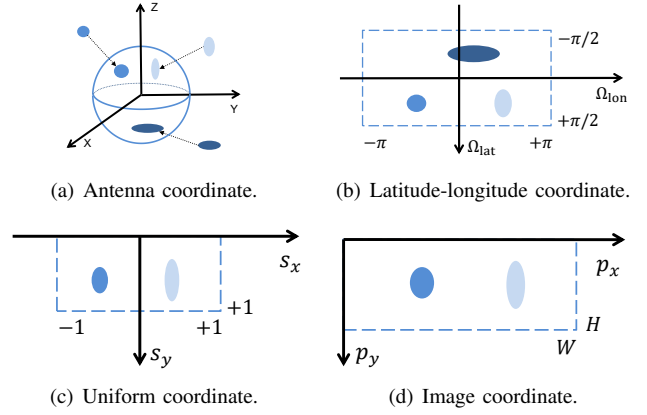


Fig. 6: The coordinate projection transformation in the projection model.

of the antenna coordinate, $\arctan 2(\cdot)$ is the 4-quadrant inverse tangent. Since we only consider signals from the upper hemisphere, we have $-\pi \leq \Omega_{\text{lon}} < \pi$ and $0 \leq \Omega_{\text{lat}} < \pi/2$, and the lower hemisphere is ignored in the following coordinate transformations. Subsequently, we convert the latitude-longitude coordinates (see Fig. 6(b)) into uniform coordinates (see Fig. 6(c)) as

$$\begin{bmatrix} s_x \\ s_y \end{bmatrix} = \begin{bmatrix} \Omega_{\text{lon}}/\pi \\ 2\Omega_{\text{lat}}/\pi \end{bmatrix}, \quad (10)$$

such that $-1 \leq s_x < 1$ and $0 \leq s_y < 1$. The final step of the projection is to transform the uniform coordinates into pixel coordinates of arbitrary resolution (see Fig. 6(d)) as

$$\begin{bmatrix} p_x \\ p_y \end{bmatrix} = \begin{bmatrix} (s_x + 1) \times W/2 \\ s_y \times H \end{bmatrix}, \quad (11)$$

where W and H represent the number of pixels contained in the width and height of the image, respectively. Considering a one-degree angular resolution, we set $W = 360$ and $H = 90$.

Through the above coordinate transformations, we maintain the relationship between the signal angles, ensuring that each pixel value in the spatial spectrum corresponds to the AoA of the signal. This allows us to calculate the signals arriving in each direction at the RX antenna array in the next subsection.

D. Electromagnetic Splatting

After the coordinate projection transformation, the 3D Gaussians representing the virtual TXs are mapped onto the 2D plane. Note that each 2D Gaussian may cover multiple pixels. In other words, the value of each pixel is the result of the combined contributions from multiple 2D Gaussians. Therefore, the role of electromagnetic splatting module is to efficiently compute the value of each pixel in the 2D plane, which is then utilized to reconstruct the spatial spectrum.

As illustrated in Fig. 7, electromagnetic splatting incorporates the EM wave propagation into the differentiable rasterization algorithm [10]. To facilitate fast parallel computing, we group adjacent pixels into non-overlapping “tiles” that can be computed independently, as depicted in Fig. 7(a). For each 2D Gaussian, we first determine which tiles it covers, duplicate the Gaussian, and assign the copies to the corresponding tiles.

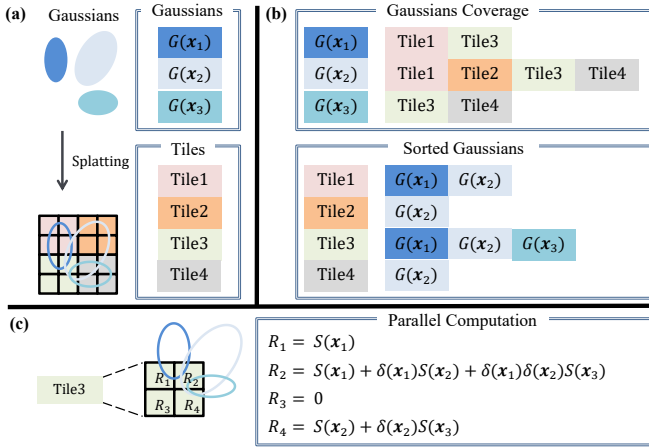


Fig. 7: An illustration of electromagnetic splatting. (a) The 3D Gaussians are splatted onto a 2D plane, and the plane is divided into non-overlapping tiles to enable parallel computation. (b) Gaussians that cover multiple tiles are duplicated and assigned to the corresponding tiles, then sorted by depth order within each tile. (c) The value of each pixel can be calculated independently and in parallel using Eqn. (12) and Eqn. (13).

These 2D Gaussians are then sorted by depth order within each tile, as shown in Fig. 7(b). In the scenario representation network, we obtain the signal $S(x_i)$ and signal attenuation $\delta(x_i)$ of each 3D Gaussian $G(x_i)$ at an arbitrary position x_i . Assuming there are a total of N 3D Gaussians contributing to a particular angle, we can express the effect of the i^{th} Gaussian $G(x_i)$ on the RX by combining Eqn. (2) and Eqn. (7) as

$$S_i(\mathbf{x}) = \left(\prod_{j=0}^{i-1} \delta(x_j) \right) S(x_i). \quad (12)$$

Consequently, for all 3D Gaussians associated with an angle (pixel) k , the combined effect is expressed as

$$R_k = \sum_{i=1}^N S_i(\mathbf{x}). \quad (13)$$

To facilitate a more intuitive understanding of this process, we provide an illustrative example in Fig. 7(c). For the pixel value R_1 in the upper-left corner, only the signal $S(x_1)$ from $G(x_1)$ contributes, without any attenuation. For the pixel value R_2 in the upper-right corner, the contributions from $G(x_1)$, $G(x_2)$, and $G(x_3)$ must be considered. The signal from $G(x_1)$ has no attenuation, but the signals from $G(x_2)$ and $G(x_3)$ are attenuated by $\delta(x_1)$ and $\delta(x_1)\delta(x_2)$, respectively, due to the depth ordering. The computation for the remaining pixel values R_k follows a similar principle.

In simple terms, we consider each projected Gaussian as a virtual TX that can affect multiple angles, while signals from multiple virtual TXs are received at each angle. Depending on the distance of these signals to the RX, they will be attenuated to different degrees, ultimately resulting in the received signal on each angle. As explained in Section III-A, the reconstructed spatial spectrum can be represented as a spatial power distribution function, where the value is proportional to the square of the amplitude of the received signal. Therefore, by deriving the received signal on each angle from Eqn. (12) and Eqn.

(13), we obtain the spatial spectrum described in Eqn. (4), which serves as a representation of the underlying WRF.

E. Summary

The WRF-GS framework integrates physical and deep learning models to enable comprehensive environment-aware channel modeling and high-fidelity spatial spectrum synthesis. At the core of this approach lies the establishment of a connection between virtual TXs and 3D Gaussians. The scenario representation network models the spatial distribution of signal propagation and attenuation using 3D Gaussians based on input data. To transform these 3D spatial representations onto a 2D plane for further processing, we employ the Mercator map projection, ensuring accurate spatial mapping. Finally, the electromagnetic splatting module employs a parallel and efficient algorithm to compute pixel values in each direction, thereby achieving fast spatial spectrum synthesis.

V. WRF-GS IMPLEMENTATION AND EVALUATION

In this section, we implement and evaluate WRF-GS in a laboratory environment using a real-world dataset in [6].

A. Implementation

WRF-GS is implemented in a Python environment using modified custom CUDA kernels for rasterization [10] and is trained on an NVIDIA GeForce RTX 3090 GPU. Detailed settings and implementation are provided below.

Position Initialization: We use the LiDAR 3D point clouds¹ shown in Fig. 2(a) to initialize the positions of 3D Gaussian points. The reason is that the most significant signal attenuation usually occurs on the object's surface [7], which corresponds to the 3D point clouds. This initialization enables a fast convergence of WRF-GS. Besides, we adopt an adaptive density control strategy [10] to learn the position distribution of the 3D Gaussians during the training process.

Position Encoding: To improve the spatial resolution, we introduce an efficient position encoding method [5], i.e.,

$$\gamma(\mathbf{t}) = (\sin(\pi\mathbf{t}), \cos(\pi\mathbf{t}), \dots, \sin(2^L\pi\mathbf{t}), \cos(2^L\pi\mathbf{t})), \quad (14)$$

where \mathbf{t} represents the 3D coordinates of the TX and L is the order of the position encoding. For the input position encoding of P_{TX} and $G(\mathbf{x})$ in the MLPs, we set $L = 9$.

Optimization Details: In the scenario representation network, we need to train two MLPs and learn the 3D Gaussian representations using the training dataset. We adopt the Adam optimizer for network training and 3D Gaussian representation. The loss function is defined as the difference between the synthesized spatial spectrum I_{pred} and the ground truth I_{gt} , i.e.,

$$\mathcal{L} = (1 - \eta)|I_{\text{gt}} - I_{\text{pred}}| + \eta(1 - \xi(I_{\text{gt}}, I_{\text{pred}})), \quad (15)$$

where the $\xi(I_{\text{gt}}, I_{\text{pred}})$ is the structural similarity index measure (SSIM) function [23], which is used to measure the similarity between two images. In addition, $\eta = 0.2$ is a weighting factor.

¹Note that WRF-GS also works well by randomly initializing the point clouds within a specified range of space.

B. Experiment Design

Dataset. We use an open-source dataset provided in NeRF² [6] to evaluate the WRF-GS framework. This dataset was obtained in a laboratory environment, which consists of multiple tables, shelves, and several small rooms. The 3D LiDAR point clouds of the environment are shown in Fig. 2(a). The RX is equipped with a 4×4 antenna array and operated at 915MHz, while the TX is an RFID tag that sends RN16 messages repeatedly. To collect the training dataset, the position of the RX is fixed and the position of the TX is systematically varied throughout the laboratory. Each sample in the dataset consists of the TX position and the corresponding spatial spectrum measured at the RX (i.e., Eqn (4)).

Benchmarks. We compare WRF-GS with several baselines:

- **Ray Tracing** [2]: This approach emits rays from the RX through every pixel in the laboratory using the 3D LiDAR point clouds. These rays interact with objects to simulate the propagation of signal in the real world.
- **Variational Autoencoder (VAE)** [24]: VAE is commonly used to generate new data samples by mapping observed data to a continuous latent space [25]. Here, we use VAE to predict the spatial spectrum at arbitrary TX positions.
- **Deep Convolutional Generative Adversarial Network (DCGAN)** [26]: DCGAN comprises a generator and a discriminator that are trained in an adversarial manner. The generator learns to generate realistic samples to deceive the discriminator, while the discriminator aims to distinguish the real samples from the generated ones.
- **NeRF²** [6]: NeRF² is a method for spatial spectrum synthesis using the NeRF technique. After training, NeRF² can predict the spatial spectrum at arbitrary TX positions.

C. Evaluation

We first evaluate the accuracy of the spatial spectrum synthesis generated by the WRF-GS, NeRF², VAE, and ray tracing methods, as shown in Fig. 2(c). The visualization is obtained by transforming the matrix form in Eqn. (4) into a polar coordinate representation. The spatial spectrum of WRF-GS for the case when the TX is located at position P3 is a projection of the constructed WRF visualized in Fig. 2(b). The results in Fig. 2(c) show that WRF-GS achieves the best prediction accuracy, closely matching the ground truth.

Fig. 8 compares the SSIM [23] values of the synthesized spatial spectra generated by different methods. SSIM values range from 0 to 1, with higher values indicating greater similarity between the synthesized and ground truth samples. The cumulative distribution function (CDF) of SSIM illustrates the disparities between the methods and the ground truth. From Fig. 8, we see that WRF-GS outperforms the baselines. Specifically, the median SSIM values for WRF-GS, NeRF², VAE, DCGAN, and ray tracing are 0.82, 0.78, 0.70, 0.56, and 0.38, respectively. The slightly inferior performance of NeRF² is due to the challenge in enumerating the virtual TX locations along the propagation paths for integration or rendering. In contrast, the ray tracing method achieves the worst performance, as it heavily relies on accurate environmental material information.

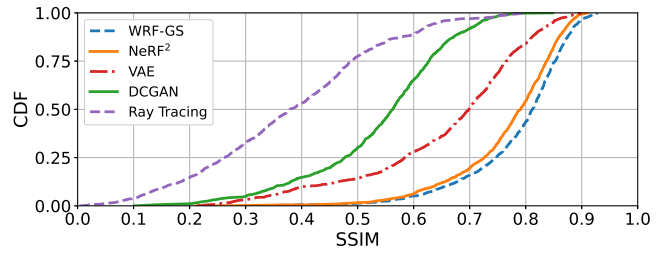


Fig. 8: The SSIM values of the synthesized spatial spectra generated by the WRF-GS, NeRF², VAE, DCGAN, and ray tracing methods.

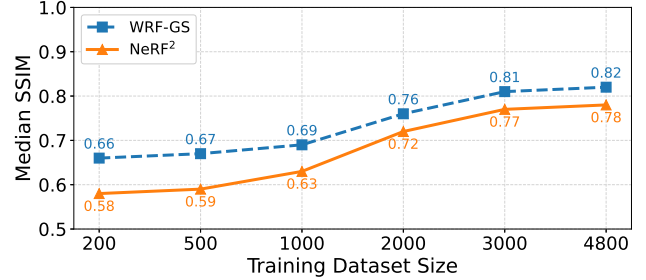


Fig. 9: The median SSIM values of the WRF-GS and NeRF² methods under different training dataset sizes.

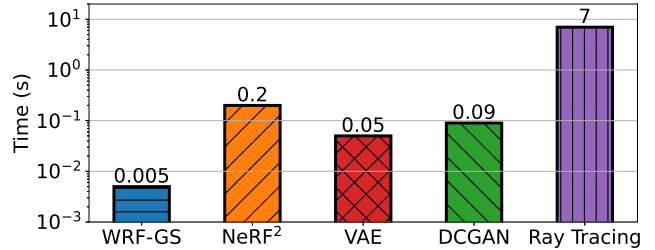


Fig. 10: The rendering time required to synthesize a spatial spectrum using different methods under the same settings.

Fig. 9 presents the median SSIM values of the WRF-GS and NeRF² methods across varying sizes of the training dataset. We maintain a consistent test dataset and randomly subsample the original training dataset to create new training datasets ranging from 200 to 4,800 samples. The results demonstrate that the WRF-GS framework consistently outperforms the NeRF² method for all training dataset sizes, improving the median SSIM by 4% to 8%. More importantly, the performance gap increases as the training dataset size decreases. This suggests that WRF-GS is well-suited for practical applications in channel modeling, as it requires less training data and, consequently, less time and effort from experienced engineers.

Fig. 10 illustrates the rendering time required to synthesize a spatial spectrum using different methods under the same settings. The results show that, for processing a single sample, WRF-GS takes 0.005s, while NeRF², VAE, DCGAN, and Ray Tracing takes 0.2s, 0.05s, 0.09s, and 7s, respectively. The processing time of WRF-GS is usually one to three orders of magnitude less than other methods. This superior computational efficiency makes WRF-GS well-suited for latency-sensitive applications.

VI. CASE STUDY: CSI PREDICTION

In this section, we demonstrate the effectiveness of WRF-GS on the downlink CSI prediction task in MIMO systems.

Typically, the downlink and uplink transmission are operated on different frequency bands in frequency domain duplex systems, where the uplink-downlink reciprocity does not hold. The base station (BS) can obtain the downlink CSI of each antenna from the uplink channel feedback by sending pilot sequences to the end devices. However, the overhead of such feedback is linearly proportional to the number of antennas and devices, making it impossible in massive MIMO systems.

Motivated by the fact that the uplink and downlink transmissions experience the same physical environment, it is reasonable to use the uplink CSI measured at the BS to infer the downlink CSI. To achieve this goal, we employ WRF-GS to predict the downlink CSI based on the uplink CSI. As pointed out in [27], each CSI is unique and highly correlated with the physical environment. Therefore, there is a mapping between the device’s location and its uplink CSI. Accounting for this, Eqn. (8) can be rewritten as

$$F_{\Theta} : (G(\mathbf{x}), I_u(\mathbf{x})) \Rightarrow (\delta(\mathbf{x}), S(\mathbf{x})), \quad (16)$$

where $I_u(\mathbf{x})$ is the uplink CSI at location \mathbf{x} . Thus, we can retrain a WRF-GS to perform the downlink CSI prediction task. In this case, the input is changed from the TX’s location to the uplink CSI, and the output is changed from the spatial spectrum to the downlink CSI.

A. Experiment Setup

We adopt the public Argos channel dataset [28] to train the MLPs and 3D Gaussian representations in WRF-GS for the downlink CSI prediction task. This dataset is collected in a real environment and the CSI is measured in different environments where a BS is equipped with 104 antennas and serves multiple users. Each CSI measurement contains 52 subcarriers. Similar to previous works [6], [17], we regard the first 26 subcarriers as the uplink channel and the remaining 26 subcarriers as the downlink channel. Apart from NeRF² [6], we also compare WRF-GS with the following three approaches:

- **FIRE** [17]: FIRE is a deep learning method based on the VAE architecture and is used to predict the downlink CSI by learning the latent distribution of the uplink CSI.
- **R2F2** [18]: Given the uplink CSI, R2F2 can obtain each path’s parameters and the number of paths by solving an optimization problem to estimate the downlink CSI.
- **OptML** [19]: OptML is a deep learning method based on the R2F2 framework and can be used to predict the underlying path information of the downlink channel.

B. Channel Estimation Accuracy

Fig. 11 depicts the prediction accuracy of the WRF-GS framework for the downlink CSI prediction task. The blue solid line represents the input ground truth uplink (GT Uplink) CSI, the orange solid line represents the ground truth downlink (GT Downlink) CSI, and the black dashed line is the predicted (Pred Downlink) CSI output by WRF-GS. It is seen that the predicted result is very close to the ground truth.

To quantify the prediction accuracy, we use the SNR metric:

$$\text{SNR} = -10 \log_{10} \left(\frac{\|C_{\text{pred}} - C_{\text{GT}}\|^2}{\|C_{\text{GT}}\|^2} \right), \quad (17)$$

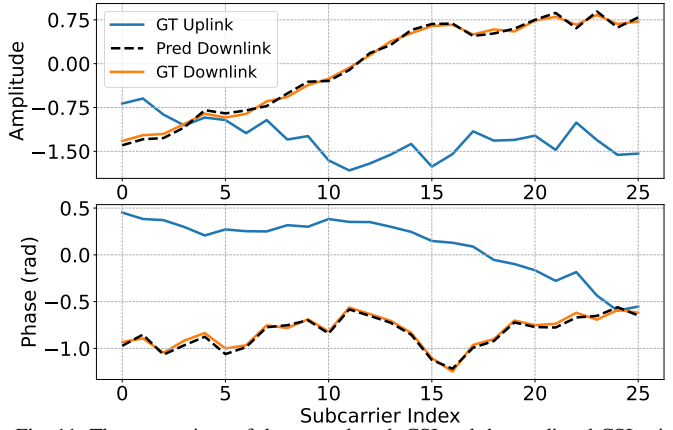


Fig. 11: The comparison of the ground truth CSI and the predicted CSI using WRF-GS in terms of the channel amplitude and phase via different sub-carriers.

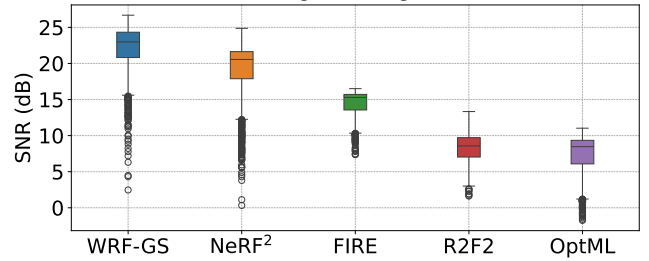


Fig. 12: The prediction accuracy of different methods in the downlink CSI prediction task. The figure shows the maximum, minimum, median, upper and lower quartile ranges of the SNR distribution for different methods, as well as the outliers. The higher the SNR, the better the prediction accuracy.

where C_{pred} is predicted downlink channel and C_{GT} is ground truth downlink channel. The higher the SNR, the better the prediction accuracy. Fig. 12 shows the SNRs of five CSI prediction algorithms. Notably, WRF-GS achieves a median SNR of 22.98 dB (10th percentile: 20.82 dB, 90th percentile: 24.33 dB). The median SNRs of NeRF², FIRE, R2F2, and OptML are 20.55 dB, 15.29 dB, 8.57 dB, and 8.47 dB, respectively. This demonstrates that WRF-GS improves the CSI prediction accuracy by efficiently modeling wireless channels.

VII. CONCLUSION

This paper introduced WRF-GS, a novel framework that combines 3D-GS and neural networks to enable fast and accurate wireless channel modeling. To adapt the 3D-GS technique from the optical domain to the RF domain, we designed three key modules for WRF-GS: a scenario representation network, a projection model, and an electromagnetic splatting technique. These modules allow WRF-GS to accurately capture the underlying physics of EM wave propagation. Remarkably, WRF-GS can synthesize new channel characteristics within milliseconds using a small number of training samples. Experimental results showed that WRF-GS outperforms existing methods in spatial spectrum reconstruction and excels in the CSI prediction task, achieving an improvement of over 2.43 dB. We envision that WRF-GS will enable various applications in future networks by leveraging its high-fidelity visualization, low sample complexity, and rapid rendering speed. The authors have provided public access to their code at <https://github.com/wenchaozheng/WRF-GS>.

REFERENCES

- [1] C. De Alwis, A. Kalla, Q.-V. Pham, P. Kumar, K. Dev, W.-J. Hwang, and M. Liyanage, "Survey on 6G frontiers: Trends, applications, requirements, technologies and future research," *IEEE Open J. Commun. Society*, vol. 2, pp. 836–886, Feb. 2021.
- [2] Z. Yun and M. F. Iskander, "Ray tracing for radio propagation modeling: Principles and applications," *IEEE Access*, vol. 3, pp. 1089–1100, Mar. 2015.
- [3] T. K. Sarkar, Z. Ji, K. Kim, A. Medouri, and M. Salazar-Palma, "A survey of various propagation models for mobile communication," *IEEE Trans. Antennas Propagation*, vol. 45, no. 3, pp. 51–82, Mar. 2003.
- [4] D. He, B. Ai, K. Guan, L. Wang, Z. Zhong, and T. Kürner, "The design and applications of high-performance ray-tracing simulation platform for 5G and beyond wireless communications: A tutorial," *IEEE Commun. Surveys Tuts.*, vol. 21, no. 1, pp. 10–27, 1st Quarter 2018.
- [5] B. Mildenhall, P. P. Srinivasan, M. Tancik, J. T. Barron, R. Ramamoorthi, and R. Ng, "Nerf: Representing scenes as neural radiance fields for view synthesis," *Commun. of the ACM*, vol. 65, no. 1, pp. 99–106, Jan. 2021.
- [6] X. Zhao, Z. An, Q. Pan, and L. Yang, "Nerf2: Neural radio-frequency radiance fields," in *Proc. ACM MOBICOM*, Madrid, Spain, 2023, pp. 1–15.
- [7] H. Lu, C. Vatheuer, B. Mirzasoleiman, and O. Abari, "Newrf: A deep learning framework for wireless radiation field reconstruction and channel prediction," in *Int. Conf. on Machine Learning (ICML)*, Vienna, Austria, 2024, pp. 1–13.
- [8] R. D. Yates, M. Tavan, Y. Hu, and D. Raychaudhuri, "Timely cloud gaming," in *Proc. IEEE INFOCOM*, Atlanta, GA, 2017, pp. 1–9.
- [9] L. Zhang, H. Sun, Y. Zeng, and R. Q. Hu, "Spatial channel state information prediction with generative AI: Towards holographic communication and digital radio twin," *arXiv preprint arXiv:2401.08023*, 2024.
- [10] B. Kerbl, G. Kopanas, T. Leimkühler, and G. Drettakis, "3D gaussian splatting for real-time radiance field rendering," *ACM Trans. on Graphics*, vol. 42, no. 4, Jul. 2023.
- [11] C. Oestges, B. Clerckx, L. Raynaud, and D. Vanhoenacker-Janvier, "Deterministic channel modeling and performance simulation of micro-cellular wide-band communication systems," *IEEE Trans. Veh. Technol.*, vol. 51, no. 6, pp. 1422–1430, Jun. 2002.
- [12] J. Tong, M. Jin, Q. Guo, and Y. Li, "Cooperative spectrum sensing: A blind and soft fusion detector," *IEEE Trans. Wireless Commun.*, vol. 17, no. 4, pp. 2726–2737, Apr. 2018.
- [13] Y. Zeng, J. Chen, J. Xu, D. Wu, X. Xu, S. Jin, X. Gao, D. Gesbert, S. Cui, and R. Zhang, "A tutorial on environment-aware communications via channel knowledge map for 6G," *IEEE Commun. Surveys Tuts.*, 4th Quarter 2024.
- [14] K. B. Letaief, W. Chen, Y. Shi, J. Zhang, and Y.-J. A. Zhang, "The roadmap to 6G: AI empowered wireless networks," *IEEE Commun. Mag.*, vol. 57, no. 8, pp. 84–90, Aug. 2019.
- [15] L. Zhang, H. Sun, J. Sun, and R. Q. Hu, "Wisegr: Dataset for site-specific indoor radio propagation modeling with 3D segmentation and differentiable ray-tracing," in *Proc. Int. on Comput., Netw. and Commun. (ICNC)*, Big Island, Hawaii, 2024, pp. 744–748.
- [16] T. Orekondy, P. Kumar, S. Kadambi, H. Ye, J. Soriaga, and A. Behboodi, "Winert: Towards neural ray tracing for wireless channel modeling and differentiable simulations," in *Proc. Int. Conf. on Learning Representations (ICLR)*, Kigali, Rwanda, 2023.
- [17] Z. Liu, G. Singh, C. Xu, and D. Vasisht, "Fire: enabling reciprocity for fdd mimo systems," in *Proc. ACM MOBICOM*, New Orleans, Louisiana, 2021, p. 628–641.
- [18] D. Vasisht, S. Kumar, H. Rahul, and D. Katabi, "Eliminating channel feedback in next-generation cellular networks," in *Proc. ACM MOBICOM*, New York, USA, 2016, pp. 398–411.
- [19] A. Bakshi, Y. Mao, K. Srinivasan, and S. Parthasarathy, "Fast and efficient cross band channel prediction using machine learning," in *Proc. ACM MOBICOM*, Los Cabos, Mexico, 2019, pp. 1–16.
- [20] Z. An, Q. Lin, P. Li, and L. Yang, "General-purpose deep tracking platform across protocols for the internet of things," in *Proc. MobiSys*, Toronto Ontario, Canada, 2020, pp. 94–106.
- [21] M. Zwicker, H. Pfister, J. Van Baar, and M. Gross, "Ewa splatting," *IEEE Trans. Vis. Comput. Graphics*, vol. 8, no. 3, pp. 223–238, Mar. 2002.
- [22] J. J. Park, P. Florence, J. Straub, R. Newcombe, and S. Lovegrove, "Deepsdf: Learning continuous signed distance functions for shape representation," in *Proc. IEEE CVPR*, Long Beach, CA, 2019, pp. 165–174.
- [23] Z. Wang, A. C. Bovik, H. R. Sheikh, and E. P. Simoncelli, "Image quality assessment: from error visibility to structural similarity," *IEEE Trans. Image Process.*, vol. 13, no. 4, pp. 600–612, Apr. 2004.
- [24] D. P. Kingma and M. Welling, "Auto-encoding variational bayes," *arXiv preprint arXiv:1312.6114*, 2013.
- [25] U. Ha, J. Leng, A. Khaddaj, and F. Adib, "Food and liquid sensing in practical environments using RFIDs," in *17th USENIX Symposium on Networked Systems Design and Implementation (NSDI 20)*. USENIX Association, 2020.
- [26] A. Radford, L. Metz, and S. Chintala, "Unsupervised representation learning with deep convolutional generative adversarial networks," *arXiv preprint arXiv:1511.06434*, 2015.
- [27] Y. Xie, J. Xiong, M. Li, and K. Jamieson, "md-track: Leveraging multi-dimensionality for passive indoor Wi-Fi tracking," in *Proc. ACM MOBICOM*, Los Cabos, Mexico, 2019, pp. 1–16.
- [28] C. Shepard, J. Ding, R. E. Guerra, and L. Zhong, "Understanding real many-antenna MU-MIMO channels," in *Proc. Asilomar Conf. on Signals, Syst. and Comp.*, Pacific Grove, CA, 2016, pp. 461–467.